SnS_2/g-C_3N_4/Graphite Nanocomposites as Durable Lithium-Ion Battery Anode with High Pseudocapacitance Contribution

Yong Zuo,[+,a,b] Xijun Xu,[+,c,d] Chaoqi Zhang,[a,b] Junshan Li,[a,b] Ruifeng Du,[a,b] Xiang Wang,[a,b] Xu Han,[e] Jordi Arbiol,[e,f] Jordi Llorca,[g] Jun Liu,*[,c,d] Andreu Cabot *[,a, f]

[a] Catalonia Institute for Energy Research – IREC, Sant Adrià de Besòs, Barcelona, 08930 (Spain)

[b] Departament d'Enginyeria Electrònica i Biomèdica, Universitat de Barcelona 08028 Barcelona (Spain)

[c] Guangdong Provincial Key Laboratory of Advanced Energy Storage Materials, School of Materials Science and Engineering, South China University of Technology, Guangzhou 510641 (P. R. China)

[d] State Key Laboratory of Pulp and Paper Engineering, South China University of Technology, Guangzhou 510641 (P. R. China)

[e] Catalan Institute of Nanoscience and Nanotechnology (ICN2), CSIC and BIST, Campus UAB, Bellaterra, 08193 Barcelona (Spain)

[f] ICREA, Pg. Lluís Companys 23, 08010 Barcelona (Spain)

[g] Institute of Energy Technologies, Department of Chemical Engineering and Barcelona Research Center in Multiscale Science and Engineering, Universitat Polittècnica de Catalunya, EEBE, 08019 Barcelona (Spain)

[+] These authors contributed equally to this work.

Abstract: Tin disulfide is a promising anode material for Li-ion batteries (LIB) owing to its high theoretical capacity and the abundance of its composing elements. However, bare SnS_2 suffers from low electrical conductivity, which results in poor rate performance and cycling stability. Herein, we present a solution-based strategy to grow SnS_2 nanostructures within a matrix of porous g-C_3N_4 (CN) and high electrical conductivity graphite plates (GPs). We test the resulting nanocomposite as anode in LIBs. First, SnS_2 nanostructures with different geometries are tested, to find out that thin SnS_2 nanoplates (SnS_2-NPLs) provide the highest performances. Such SnS_2-NPLs, incorporated into hierarchical SnS_2/CN/GP nanocomposites, display excellent rate capabilities (536.5 mAh g^{-1} at 2.0 A g^{-1}) and an outstanding stability (~99.7 % retention after 400 cycles), which are partially associated with a high pseudocapacitance contribution (88.8 % at 1.0 mV s^{-1}). The excellent electrochemical properties of these nanocomposites are ascribed to the synergy created between the three nanocomposite components: i) thin SnS_2-NPLs provide a large surface for rapid Li-ion intercalation and a proper geometry to stand volume expansions during lithiation/delithiation cycles; ii) porous CN prevents SnS_2-NPLs aggregation, habilitates efficient channels for Li-ion diffusion and buffer stresses associated to SnS_2 volume changes; and iii) conductive GPs allow an efficient charge transport.

Keywords: Nanocomposite, Li-ion battery, anode, tin disulfide, pseudocapacitance

1. Introduction

Lithium-ion batteries (LIBs) are widely commercialized for portable applications owing to their notable volumetric energy density and their flexible and lightweight design. However, commercial devices suffer from low stability, and their potential energy densities and charging rates are far from those potentially attained by LIBs, which leaves plenty of room for improvement of their design and components, particularly of their anode materials.[1–3] Commercial LIBs use graphite anodes, which provide a modest theoretical energy density, 372 mAh g^{-1},[4,5] and are far away from the requirements of the next generation of high-energy and high-power LIBs.[6] Therefore, alternative anodes based on Si,[7,8] Ge [9,10] or Sn[11–13] are being actively developed.

Among the different materials able to intercalate or react with Li^+, sulfides and particularly SnS_2 are especially interesting due to the abundance of its elements and the ability to simultaneously interact with Li^+ through two different bulk mechanisms: Li-S reaction and Sn-Li alloying. SnS_2 anodes have a potential capacity of 1231 mAh g^{-1} ascribed to the combination of the Li-S reaction ($SnS_2 + 4Li^+ + 4e^- \rightarrow Sn + 2Li_2S$, 586 mAh g^{-1} capacity contribution)[14] and the Sn-Li alloying/dealloying reaction ($Sn + 4.4Li^+ + 4.4e^- \rightarrow Li_{4.4}Sn$, 645 mAh g^{-1} capacity contribution).[15,16] Besides, oxides and chalcogenides may provide a significant additional energy storage capacity contribution in the form of a rapid surface-related pseudocapacity.[3,17,18]

SnS_2 displays a two-dimensional (2D) hexagonal structure with layers of tin atoms sandwiched between two close-packed layers of sulfur atoms. Adjacent sandwiches, separated a distance of 0.59 nm, are hold together by Van der Waals forces.[19–21] This layered structure allows for the effective and fast diffusion of Li^+ (0.076 nm) to interact with Sn and S. However, during charge/discharge processes, SnS_2 suffers from huge volumetric changes in large part related to the expansion/contraction in the c direction, i.e. across the planes, its softer crystallographic direction. This volumetric changes may result in the pulverization and detachment of the material from the current collector.[22–24] Additionally, the low electrical conductivity of SnS_2 provides a poor rate performance. These limitations lead to a deficient cyclability, especially at high current densities.[25–28]

To overcome its flaws as anode material in LIBs, SnS_2 needs to be nanostructured[29–32] and combined with high surface area materials, e.g. carbon-based networks, to improve dispersion and simultaneously provide the necessary paths for electrolyte diffusion and electron transport.[33–35] Graphene is considered as one of the best materials for these last roles,[25,36] owing to its large surface, extraordinary electrical conductivity, and convenient flexibility that allows accommodating the conductive network to the volume expansion of the active material.[37] Graphene can interact with Li^+ itself, delivering additional storage capacity. To maximize this interaction, graphene can be doped with large concentrations of N atoms which interact more efficiently with Li^+ due to the higher

electronegativity of nitrogen compared with carbon.[38–40] In this direction, graphitic carbon nitride (g-C_3N_4, CN) is regarded as the analogue to graphite with the highest level of nitrogen, and thus may provide a significant Li^+ storage capacity. [6,41,42] CN also has a 2D layered structure in which p-conjugated graphitic planes are composed by alternate arrangements of sp2 hybridized carbon and nitrogen atoms.[43,44] Advantageously, CN can be easily produced in a scalable way by the thermal decomposition of urea at moderate temperatures.[45,46] However, such CN is usually characterized by a low electrical conductivity due to an intrinsic porous microstructure.[41,47] Thus a highly conductive material needs to be additionally introduced to provide the necessary paths for electron transport.

Herein, we combine SnS_2 nanostructures with high surface area and porous CN and high electrical conductivity graphite plates (GPs) in hierarchical nanocomposites, and analyze their performance as anode material in LIBs. We initially identify the SnS_2 nanostructure geometry providing better electrochemical performance by producing and testing SnS_2 particles with different shapes. The better performing SnS_2 nanostructure is then combined with porous CN, which we demonstrate is able to improve to some extent the electrode cycling stability. Finally, we analyze the effect of additionally incorporating conductive GP into the mixture to further improve performance.

2. Experimental section

Chemicals: Tin(IV) chloride pentahydrate ($SnCl_4 \cdot 5H_2O$, 98%), sulfur powder (99.8%), tetrahydrofuran (THF, ≥99%), and GP (99 % carbon basis, -325 mesh) were purchased from Sigma-Aldrich. 1-octadecene (ODE, 90%) was purchased from Alfa-Aesar. Oleylamine (OAm, 80-90%), oleic acid (OAc, 70%), and urea (99 %) were purchased from Acros. Super P, polyvinylidene fluoride (PVDF) and porous polypropylene film (Celgard2400) were purchased from Shenzhen Kejing Star Technology Co. LTD. N-methy1-2-pyrrolidone (NMP, 99%), ethylene carbonate (EC), diethylcarbonate (DEC) and fluoro ethylenecarbonate (FEC) were purchased from Aladdin. Toluene, hexane, isopropanol and ethanol were of analytical grade and obtained from various sources. GPs were cleaned using diluted HCl and ethanol under sonication. All other chemicals were used as received, without additional purification. Aqueous solutions were prepared using Milli-Q water (DW, 18.2 MΩ·cm).

Synthesis of SnS_2 nanostructures and SnS_2/CN and SnS_2/CN/GP nanocomposites: Plate- and flower-shaped SnS_2 nanostructures were produced following our recently reported protocol.[21] Briefly, to prepare SnS_2 nanoplates (SnS_2-NPLs), $SnCl_4 \cdot 5H_2O$ (2 mmol), ODE (16 mL), OAc (4 mL), OAm (2 mL) and THF (1 mL) were added into a three-neck round flask (50 mL). The solution was stirred using a magnetic stirring bar and a syringe was inserted into the solution to bubble Ar. The solution was then heated up to 140 °C and kept at this temperature for 1h to remove low boiling-point impurities. Then the obtained brown transparent solution was heated to 220 °C. At this temperature, 4 mL of S-OAm stock solution, prepared by dissolving sulfur powder (4 mmol) into OAm (4 mL) under sonication, were quickly injected into the reaction flask with a syringe. The solution was maintained at 220 ºC for 1h after S source injection and afterward quickly cooled down using a cold-water bath. The resulted product was centrifuged at 6000 rpm for 4 mins after adding toluene (15 mL), and then washed three times with toluene and ethanol by dispersion-precipitation cycles. The obtained yellow products (~80 % yield for SnS_2-NPL) were dried under vacuum for posterior use and characterization.

SnS_2 microflowers (SnS_2-MFL) were prepared in the same way, but replacing OAm with ODE. The S-ODE stock solution was prepared by dissolving sulfur powder (4 mmol) into ODE (4 mL) under Ar at 180 ºC in a 25 mL flask.

SnS_2/CN and SnS_2/CN/GP nanocomposites were prepared by adding CN (25 mg) and eventually GP (25 mg) into the reaction mixture containing enough Sn and S precursor to nominally yield 2 mmol SnS_2. The precursor solution was initially stirred for 30 min at room temperature to ensure a proper dispersion of the carbon-based materials. The exact same reaction conditions used to prepare unsupported SnS_2 nanostructures were applied to prepare SnS_2/CN and SnS_2/CN/GP nanocomposites**.**

Synthesis of CN: CN was prepared according to a method reported previously with some modification.[45,46] Briefly, 2 g of urea was placed in a crucible with a loosely closed lid, and heated to 550 °C at a rate of 5 °C/min for 4 h in a tubular furnace with air flow. The obtained light yellow product was collected after cooling down to room temperature and grounded into powder. To hydrolyze the bulk CN in alkaline conditions, 500 mg of as-synthesized powder was mixed with 20 mL of NaOH solution (3 M in DW). The mixture was stirred at 70 °C for 8 h. The obtained hydrolyzed CN was washed using water/ethanol and collected using centrifugation for three times. The product was finally dried under vacuum and stored until further use**.**

Ligand removal (LR): Native organic ligands were removed from the SnS_2 surface according to previously published reports.[48,49] Briefly, SnS_2 particles were dispersed in a vial containing a solution of 0.8 mL hydrazine and 25 mL acetonitrile. The mixture was then stirred for 4 h at room temperature and subsequently collected by centrifugation. The resulted product was further washed with acetonitrile and centrifuged at 2000 rpm for additional 2 times. Ligand-removed products were collected and stored in Ar atmosphere after drying under vacuum at room temperature.

Sample characterization: Powder X-ray diffraction (XRD) patterns were obtained on a Bruker AXS D8 ADVANCE X-ray diffractometer operating at 40 kV and 40 mA with Ni-filtered (2 μm thickness) Cu Kα1 radiation (λ = 1.5406 Å). X-ray photoelectron spectroscopy (XPS) was carried out on a SPECS system equipped with an Al anode XR50 source operating at 150 W and a Phoibos 150 MCD-9 detector. The pressure in the analysis chamber was kept below 10^{-7} Pa. Data processing was performed with the CasaXPS program. Binding energy (BE) values were centered by using the C 1s peak at 284.8 eV. SEM analysis was carried out in a ZEISS Auriga microscope with an energy dispersive X-ray spectroscopy (EDX) detector at 20 kV to study composition. Transmission electron microscopy (TEM) characterization was carried out on a ZEISS LIBRA 120, operating at 120 kV. High-resolution TEM (HRTEM) images were obtained using a field emission gun FEI Tecnai F20 microscope at 200 kV with a point-to-point resolution of 0.19 nm. High angle annular dark-field (HAADF) STEM was combined with electron energy loss spectroscopy (EELS) in the Tecnai microscope by using a GATAN QUANTUM filter. For TEM characterization, samples were prepared by drop casting a dispersion containing the material on a 200 mesh copper grid. Thermogravimetric (TG) analyses were performed using a PerkinElmer Diamond TG/DTA instrument. Samples were measured in air at a heating rate of 5 ºC/min from ambient temperature to 800 ºC. Fourier transform infrared spectroscopy (FTIR) was performed on an Alpha Bruker FTIR spectrometer with a platinum attenuated total reflectance (ATR) single reflection module. FTIR data were typically averaged over 24 scans.

Electrochemical measurements: To evaluate the electrochemical performance of the materials, 80 wt% of sample, 10 wt% Super P, and 10 wt% PVDF were mixed together in an appropriate amount of NMP to form a homogenous slurry. Subsequently, the resultant flowing slurry was coated on Cu foil and dried in a vacuum oven at 80 ºC for 24 h. The foil was then cut into disks with a diameter of 12 mm. The mass of active material was estimated to be *ca.* 1.0 mg/cm^2. To test the performance of obtained electrodes, half cells were constructed in an argon-filled glove-box (H_2O and O_2 < 0.1 ppm) using Celgard2400 as separator, and $LiPF_6$ solution (1 M) in EC/DEC (1:1 volume) with 5 wt% FEC as the electrolyte. Galvanostatic charge-discharge curves of the assembled cells were measured at different current densities in the voltage range of 0.01-3.0 V versus Li^+/Li on a battery test system (CT2001A, LAND). Cyclic voltammetry (CV) measurements were respectively performed with an electrochemical workstation (Gamry Interface 1000) in the voltage range from 0.01-3.0V and the scan rate from 0.1 to 1mV s^{-1}. Electrochemical impedance spectroscopy (EIS) tests were performed in a scanning frequency range from 100 kHz to 10 mHz using a sinusoidal voltage with amplitude of 5 mV.

3. Results and discussion

Figure 1 shows electron microscopy micrographs of SnS_2 nsnostructures, CN and GP. Following the above detailed procedure, SnS_2-NPLs with ~200 nm in diameter and ~10 nm thickness, and ~1 μm SnS_2-MFLs were produced (Figures 1a and 1b).[21] CN showed a graphene-like flexible morphology with high porosity (Figure 1c and inset) and GP was characterized by a surface-smooth thick plate morphology (Figure 1d). Figure 1e shows a SEM micrograph of a SnS_2-NPL/CN/GP nanocomposite formed by growing SnS_2-NPLs in the presence of CN and GP. Notice that the morphology of CN and GP was not modified during the synthesis process, although their particle size was slightly reduced as they were probably fragmented during agitation. Besides, the presence of CN and GP in the reaction mixture did not significantly change the size and morphology of the obtained SnS_2-NPLs. Additional SEM micrographs of SnS_2/CN and SnS_2/CN/GP nanocomposites obtained from SnS_2-NPLs and SnS_2-MFLs can be found in Figure S1, demonstrating the presence of SnS_2 in all the nanocomposites.

Figure 1f shows the XRD patterns of SnS_2-NPLs, SnS_2-MFLs, CN and GP. XRD patterns of the SnS_2/CN/GP composites can be found on Figure S2a. XRD patterns of GP and CN displayed two characteristic peaks, corresponding to the (002) and (004) crystallographic planes for GP and the (100) and (002) for CN. The XRD pattern of SnS_2 could be indexed with the hexagonal berndtite SnS_2 structure (JCPDS# 23-0677). The high intensity ratio between (001) and (101) XRD peaks for SnS_2-NPL in comparison with SnS_2-MFL, pointed at the highly asymmetric morphology of SnS_2-NPL with largely exposed {001} facets. The XRD pattern of SnS_2/CN/GP was also indexed with the berndtite SnS_2 structure, with the two additional peaks of GP. The diffraction peaks of CN were not visible in the XRD pattern of SnS_2/CN/GP because of their low intensity and their partial overlap with those of SnS_2. HRTEM micrographs (Figure S2b) confirmed the hexagonal structure of SnS_2 NPLs (space group = P-3M1).

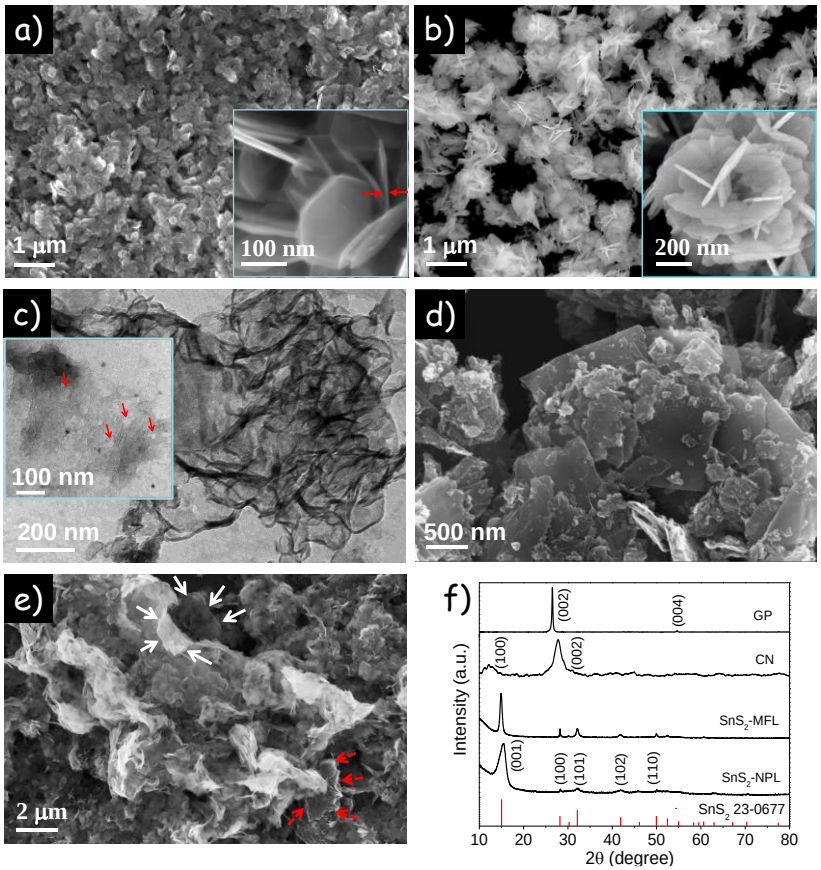

Figure 1. a) SEM micrograph of SnS_2-NPLs. b) SEM micrograph of SnS_2-MFLs. c) TEM micrograph of CN. In the inset, arrows point out at the presence of pores/holes. d) SEM micrograph of GP. e) SEM micrograph of a SnS_2-NPL/CN/GP composite. White arrows point at a CN structure. Red arrows point at SnS_2-NPLs. f) XRD pattern of SnS_2-NPLs, SnS_2-MFLs, CN and GC.

Figure 2a displays SEM-EDX maps of the different elements within SnS_2/CN/GP, showing a homogenous distribution of the different components within the composite. EDX analysis additionally showed the SnS_2 composition to be slightly sulfur rich, with an elemental ratio of S/Sn = 2.06 (Figure S3). EELS elemental maps revealed a homogenous distribution of N at the nanometer level, proving CN nanosheets to ubiquitously support/wrap SnS_2 nanostructures (Figure 2b).

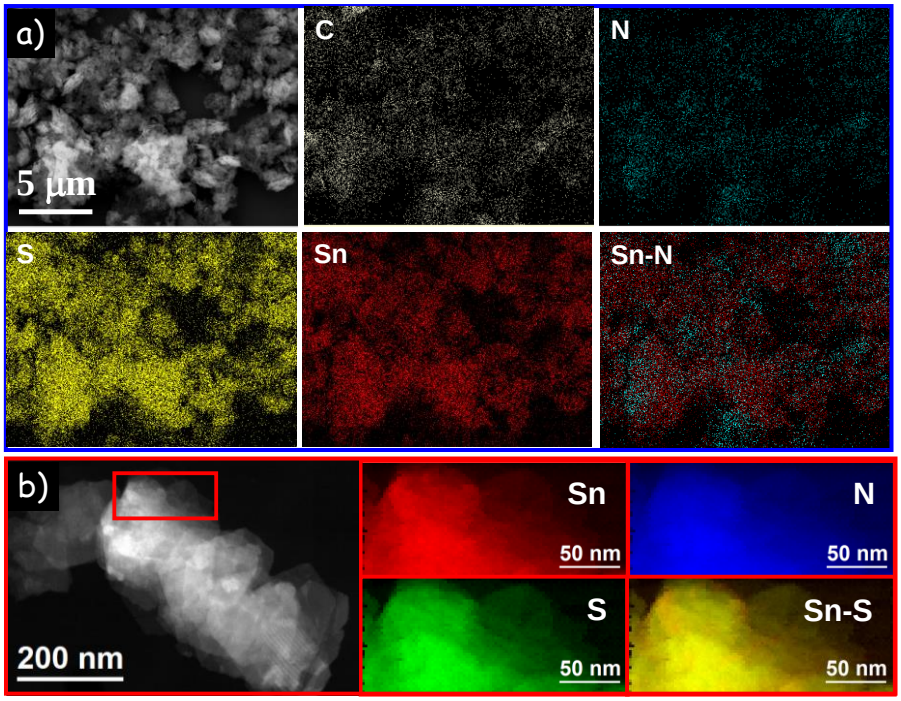

Figure 2. a) SEM micrograph and EDX elemental maps of a SnS_2/CN/GP composite. b) STEM micrograph of a SnS_2/CN/GP composite and EELS chemical composition maps obtained from the red squared area in the STEM micrograph.

The bulk content of CN, GP and SnS_2 within SnS_2/CN/GP composites was measured using TGA (Figure S4). Upon heating the sample up to 800 ºC in the presence of oxygen, the composite displayed a total weight loss of 34 %. This weight loss was ascribed to the oxidative dissociation of GP and CN, the oxidation of SnS_2 to SnO_2 and the removal of surface ligands.[50] TGA of SnS_2-NPLs provided a final mass of SnO_2 of a 77 % with respect to the initial amount of material analyzed, which corresponded to an initial content of SnS_2 in the SnS_2-NPLs sample of 93.4 %. We hypothesize the remaining 6.6 wt% to be associated with surface organic ligands. From the weight decrease measured in SnS_2/CN/GP composites (66 % SnO_2 remaining, which corresponds to 80.1 % initial SnS_2), and assuming the same ratio of organic ligands as in SnS_2-NPLs, the total amount of CN and GP with respect to SnS_2 was estimated at a 17.7 % (14.2 wt%/80.1 wt%), which was close to the nominal 17.1 % [50 mg/(183*2*80%) mg].

SnS_2/CN/GP nanocomposites were treated with a mixture of hydrazine and acetonitrile to remove the surface ligands from the final composites (see Experimental section for details).[48,49] FTIR analyses confirmed the successful ligand removal from the material (Figure S5). XPS analysis of SnS_2-based composites after hydrazine treatment showed the surface of the final material to be slightly reduced (Figure 3). Two chemical environments were clearly visible in the Sn 3d XPS spectrum (Figure 3a) of the SnS_2/CN/GP composites. The first doublet (Sn $3d_{5/2}$ at 487.1 eV) was associated with Sn^{4+},[51,52] and the second doublet (Sn $3d_{5/2}$ at 485.8 eV) with Sn^{2+}.[53,54] From the peak intensities, we estimated the ratio

of the two chemical states to be ca. Sn^{2+}/Sn^{4+} = 0.3. Similarly, the XPS spectrum of the S 2p region (Figure 3b) of the SnS_2/CN/GP composites was fitted with two doubles. The first was located at 162.1 eV (S $2p_{3/2}$) and 163.3 eV (S $2p_{1/2}$), and it was associated with S^{2-} in the SnS_2 lattice.[51,52,55] A second S 2p doublet was fitted at 160.7 eV (S $2p_{3/2}$) and 161.8 eV (S $2p_{1/2}$), and it was associated with S^{2-} within SnS.[53,54] As measured by XPS, the surface ratio SnS/SnS_2 = 0.4. The N 1s spectrum of SnS_2/CN/GP (Figure 3c) showed three peaks at BEs of 398.2 eV, 399.2 eV and 401.0 eV, which were assigned to N-(C-N=C), tertiary nitrogen N-(C)3 group and C-N-H of CN, respectively.[56,57] Finally, the C 1s spectrum (Figure 3d) showed 2 to 3 characteristic peaks corresponding to carbon within CN and graphitic carbon.[58] No clear evidence of chemical bonding between CN, GP and SnS_2 could be obtained by XPS.

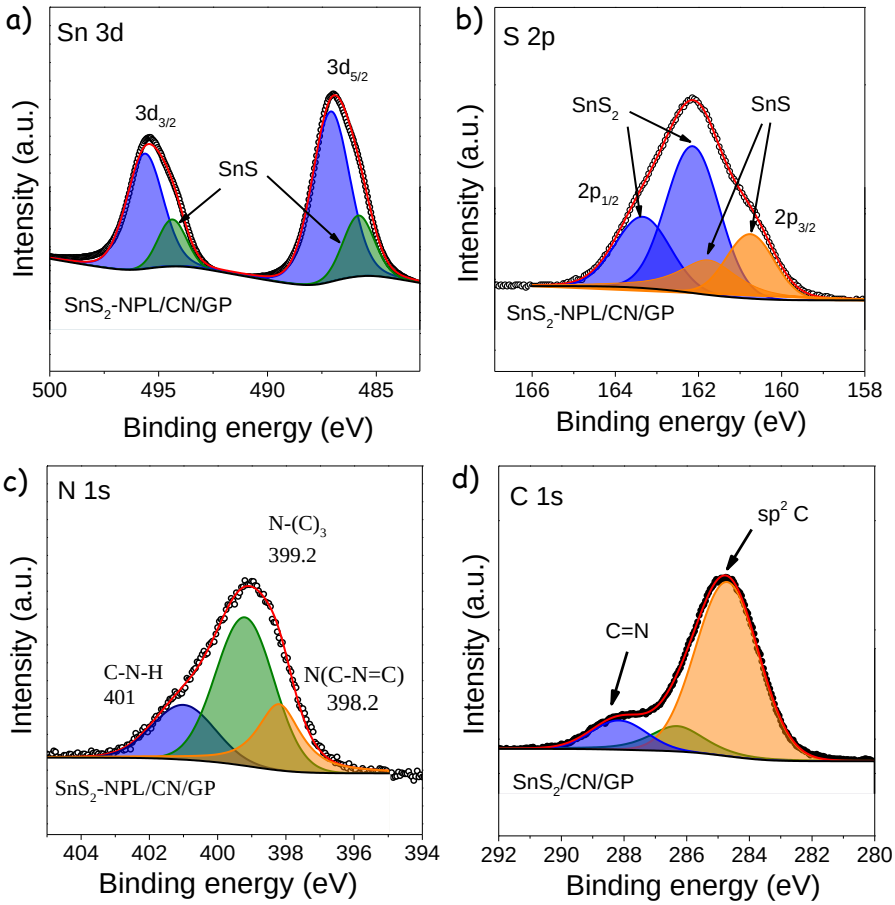

Figure 3. XPS spectra of a) Sn 3d region; b) S 2p region; c) N 1s region and d) C 1s region of SnS_2/CN/GP.

The electrochemical behavior of SnS_2-based LIB anodes was initially investigated using CV with a scan rate of 0.1 mV s^{-1} in the voltage window 0.01-3 V vs. Li^+/Li. To determine the best performing SnS_2

nanostructure geometry, SnS_2-NPL and SnS_2-MFL were initially compared. Figure 4a shows results obtained from a SnS_2-NPL electrode. The first sweep displayed three clear cathodic current peaks at ~1.8 V, ~1.1 V and ~0.15 V. The peak at ~1.8 V disappeared in the following cycles, and it was assigned to lithium insertion in the layered SnS_2 without phase decomposition (equation 1).[52,59,60] The strong peak at ~1.1 V was attributed to the decomposition of SnS_2 (equation 2), the formation of Li_2S and Sn metal (equation 3), and the growth of the solid electrolyte interface (SEI) layer.[52,61,62] The intensity of this peak decreased and was shifted to ~1.3 V in subsequent cycles.[52,63] The cathodic peak at ~0.15 V corresponded to the reaction between metallic Sn and Li^+ (equation 4). [61,63] Anodic peaks at ~0.5 V, ~1.25 V, and ~1.8 V were related to the dealloying reaction of $Li_{4.4}Sn$ to metallic Sn, the partial deinsertion reaction of Li^+ from Li_xSnS_2 to form SnS_2, and the oxidation of metallic Sn to SnS_2, respectively.[22, 64–66] In addition, the anodic peak at ~2.35 V was assigned to the transformation of unreacted Li_2S to polysulfides.[67,68] Very similar CV profiles were obtained for SnS_2-MFL anodes (Figure 4b). The aforementioned electrochemical reactions between SnS_2 and lithium ions during charge-discharge processes are outlined as follows:

$$SnS_2 + xLi^+ + xe^- \rightarrow Li_xSnS_2 \quad (1)$$

$$Li_xSnS_2 + (4-x)Li^+ + (4-x)e^- \rightarrow 2Li_2S + Sn \quad (2)$$

$$SnS_2 + 4Li^+ + 4e^- \rightarrow Sn + 2Li_2S \quad (3)$$

$$Sn + 4.4Li^+ + 4.4e^- \rightarrow Li_{4.4}Sn \quad (4)$$

Galvanostatic charge-discharge curves of the SnS_2-NPL and SnS_2-MFL electrodes were performed in the voltage range of 0.01-3.0 V *vs.* Li^+/Li at a current density of 0.1 A g^{-1} (Figure 4c,d). Similar profiles were obtained for SnS_2-based electrodes with different particle geometries. The initial irreversible capacity loss was mainly associated with the decomposition of electrolyte on the surface of active particles to form the SEI layer among other possible irreversible processes (Figure 4c,d).[69,70]

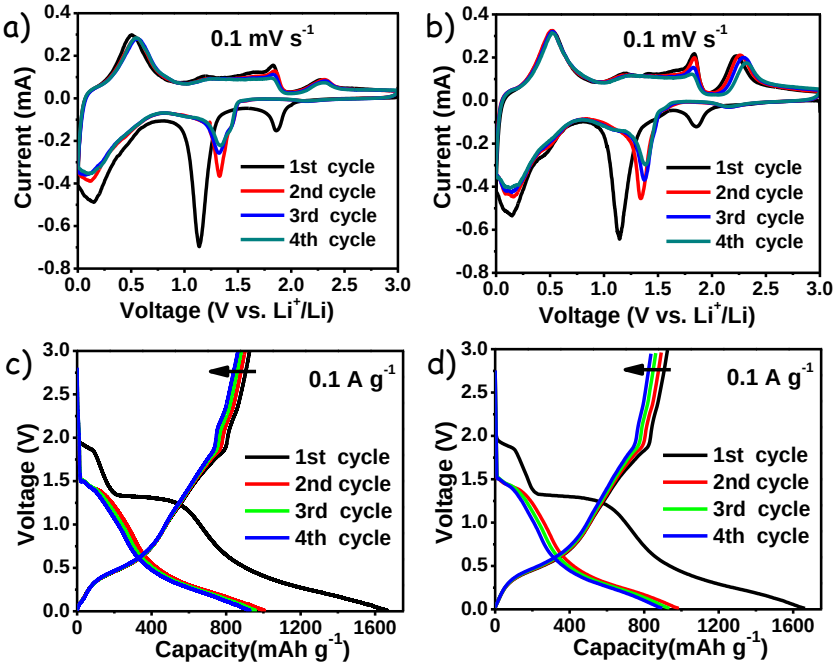

Figure 4. Initial four CV curves obtained at a scan rates of 0.1 mV s^{-1} on electrodes of a) SnS_2-NPL; b) SnS_2-MFL. Initial four galvanostatic charge-discharge curves obtained at a current density of 0.1 A g^{-1} on electrodes of c) SnS_2-NPL; d) SnS_2-MFL.

As shown in Figure 5, SnS_2-NPL electrodes provided significantly better rate capacity performance than SnS_2-MFL, with a lower loss of reversible capacity as the current density increased. SnS_2-NPL electrodes delivered a capacity of ~380 mAh g^{-1} after increasing a 50 fold the current density, from 0.1 A g^{-1} to 5.0 A g^{-1}, ~59 % of the initial capacity was recovered when the current density decreased back to 0.1 A g^{-1}. By contrast, SnS_2-MFL electrodes delivered a lower capacity of only ~70 mAh g^{-1} and ~17 % recovery. These results pointed at SnS_2-NPL as the best SnS_2 nanostructure geometry to be used as LIB anode material. Therefore, additional work was carried out using SnS_2-NPLs.

Figure S6a,b displays CV data obtained from electrodes based on SnS_2/CN and SnS_2/CN/GP nanocomposites. The first CV cycle of SnS_2/CN and SnS_2/CN/GP electrodes displayed similar CV profiles as those obtained for SnS_2 electrodes, except that SnS_2/CN/GP electrodes showed stronger intensity peaks related to conversion and alloying reactions, indicating a better cycling performance. Figure S6c,d shows the galvanostatic charge-discharge performance of electrodes based on SnS_2/CN and SnS_2/CN/GP in the voltage range of 0.01-3.0 V *vs.* Li^+/Li at a current density of 0.1 A g^{-1} (Figure S6c,d). The initial irreversible capacity loss can be ascribed to the formation of the SEI layer.[69,70]

The rate performance, charge-discharge curves and charge-discharge capacity of electrodes based on SnS_2/CN and SnS_2/CN/GP were further analyzed to assess their stability (Figure 5). SnS_2/CN/GP

electrodes provided better rate capacity performance than SnS_2/CN and SnS_2 electrodes, with reversible capacities moderately decreasing as the current densities increased. Namely, SnS_2/CN/GP electrodes delivered a capacity of ~470 mAh g^{-1} after increasing the current density from 0.1 A g^{-1} to 5.0 A g^{-1}, and ~74 % of the initial capacity was recovered when the current density decreased back to 0.1 A g^{-1}. By contrast, SnS_2/CN and SnS_2-NPL electrodes delivered lower capacities of ~280 mAh g^{-1} (~68% recovery) and ~380 mAh g^{-1} (~59 % recovery), respectively.

The charge-discharge capability of the electrodes based on bare SnS_2 notably decreased with the cycling process, which was attributed to the progressive disconnection of the particles from the current collector associated to the large volume change during Li^+ insertion/deinsertion.[71–73] The poor electrical conductivity of SnS_2 rendered an inhomogeneous reaction with Li^+, resulting in a non-uniform volumetric changes that created additional stress. This stress promoted cracking of the particles and it thus resulted in a larger degradation of capacity. This drawback was particularly severe at higher current densities of charge-discharge, thus deteriorating the rate performance.[71] On the other hand, the presence of CN allowed to maintain the capacity after activation, which we associated to the role played by CN as spacer to accommodate the volumetric expansion within SnS_2 and to alleviate the detachment of the SnS_2-NPL.[73–75] Besides, the interconnected porous structure of CN could provide continuous paths for Li-ion diffusion to the active material.[75–77]

SnS_2/CN/GP composites demonstrated even better stability towards Li-ion charge-discharge processes, with a capacity of 571 mAh g^{-1} (~99.3 % capacity retention) and 99.4 % coulombic efficiency at 1.0 A g^{-1} for 470 cycles (from 30 cycles to 500 cycles), performing much better than SnS_2 and SnS_2/CN electrodes. We attributed the improved charge-discharge performance, especially the capacity stability, to the improved charge transport with the incorporation of high electrical conductivity GPs. Besides, the changed SEI interface due to the addition of GC could also contribute. [78,79]

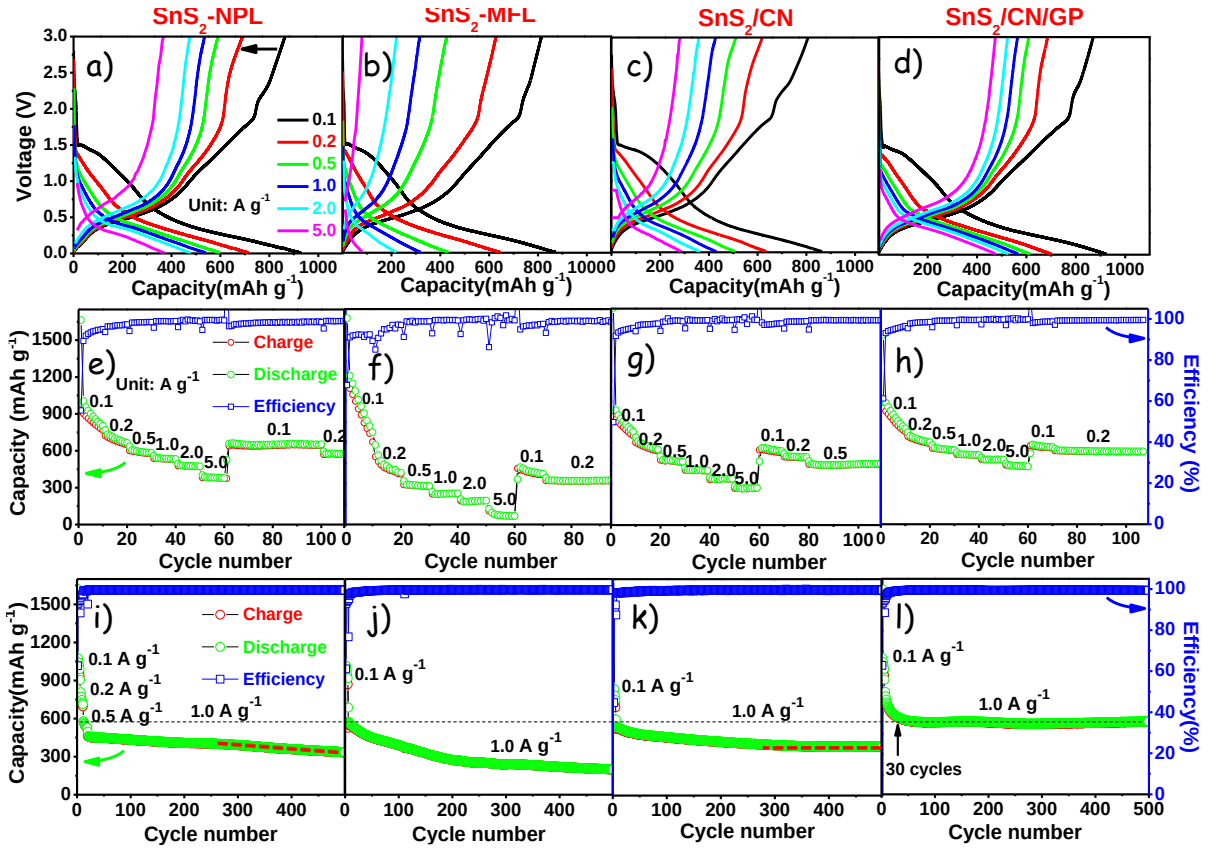

Figure 5. Li-ion storage performance of different electrodes as displayed on the top. a-d) Rate performance and e-f) charge-discharge curves at 0.1, 0.2, 0.5, 1.0, 2.0 and 5.0 A g^{-1}. i-l) Charge-discharge capacity and related efficiency curves over 500 cycles at a current density of 1.0 A g^{-1}.

Figure 6a displays EIS data obtained from electrodes containing SnS_2-NPLs and SnS_2/CN/GP. Impedance responses were fitted with an equivalent circuit containing a series resistance R_s, a charge transfer resistance R_{ct}, and a constant phase element CPE (Figure 6a, inset).[21,80] Fitting results clearly revealed an enhanced charge transfer process on SnS_2/CN/GP electrodes, with a much lower R_{ct}, 110 Ω, when compared with SnS_2, 290.8 Ω. This result was consistent with the faster charge transfer and charge-discharge kinetics.

Figure 6b shows the charge-discharge capacity and related efficiency of a SnS_2/CN/GP electrode during long-term charge-discharge cycling at a high current density of 2.0 A g^{-1}. The electrodes displayed an outstanding capacity retention of ~99.7 % and a coulombic efficiency of 99.3 % after 400 charge-discharge cycles (comparing cycles 30th and 430th, Table S1). While SnS_2 and SnS_2/CN electrodes displayed a very fast initial capacity decay due to the partially irreversible conversion reaction (equation 3),[81,82] the SnS_2/CN/GP electrode exhibited a capacity decay that extended during the initial 30 cycles. According to recent reports, we ascribed this relatively extended decay to the decomposition of the electrolyte catalyzed by GC.[78,79]

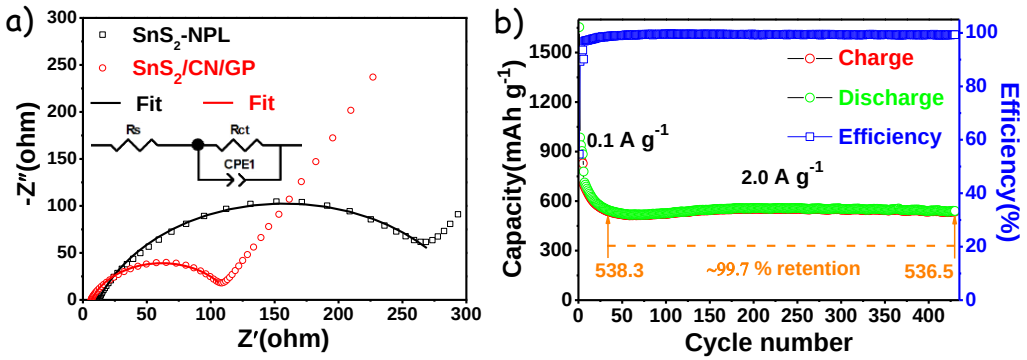

Figure 6. a) Nyquist plots of the EIS data obtained from SnS_2-NPL and SnS_2/CN/GP electrodes. b) Charge-discharge capacity and related efficiency curves of an SnS_2/CN/GP electrode over 430 cycles at a current density of 2.0 A g^{-1}. The electrode was initially activated at 0.1 A g^{-1} for 5 cycles.

To understand the reaction kinetics of the SnS_2/CN/GP electrode during charge-discharge cycling, CV measurements under different scan rates in the potential range of 0.01-3.0 V *vs.* Li^+/Li were carried out. As shown in Figure 7a, the anodic peak at 0.72 V and cathodic peak at 1.17 V increased with scan rate from 0.1 to 1.0 mV s^{-1}. The measured current (i) should increase with a power of the scan rate (ν):[3,48,83-85]

$$i = a\,\nu^{\,b} \qquad (5)$$

$$\log i = b \cdot \log \nu + \log a \qquad (6)$$

in which a and b are adjustable constants related to the reaction process. According to previous reports,[3,48,84,86,87] b = 1 corresponds to an ideal capacitive behavior, while b = 0.5 indicates a diffusion-controlled process. Generally, the capacitive behavior is particular attractive, since it is a much faster and stable process to provide relatively good rate performance and long cycle life, compared with the diffusion process.[3] Based on equation 6, the b value could be calculated by a liner fit of log i against log ν, as shown in Figure 7b. For SnS_2/CN/GP electrodes, b values of 0.80 and 0.67 were calculated at 0.72 V and 1.17 V, respectively. b values above 0.5 were consistent with a fast kinetics resulting from a significant pseudocapacitive contribution.

Total capacity at a giving scan rate was divided into a diffusion-controlled ($k_1\nu^{1/2}$) and a capacitor-like ($k_2\nu$) contribution:

$$i\,(V) = k_1\nu^{1/2} + k_2\nu \qquad (7)$$

Thus:

$$i\,(V)/\nu^{1/2} = k_1 + k_2\nu^{1/2} \qquad (8)$$

Then, k_1 and k_2 values could be calculated by plotting $i(V)/\nu^{1/2}$ versus $\nu^{1/2}$.[3,48,83,85,88] Figures 7c and 7d show the capacitive contribution to the total capacity. Very high pseudocapacitive contributions of 65.3 %, 69.4 %, 75.6 %, 82.5 % and 88.8% at scan rates of 0.1, 0.2, 0.4, 0.7 and 1.0 mV s^{-1}, respectively, were obtained (Figure 7d). Electrodes based on SnS_2-NPL, SnS_2-MFL and SnS_2/CN showed lower pseudocapacitive contributions than those of SnS_2/CN/GP electrodes at all scan rates measured (Figure S8). The high pesudocapacitance of SnS_2/CN/GP electrodes was in large part related to their large surface areas derived from their hierarchical structure.

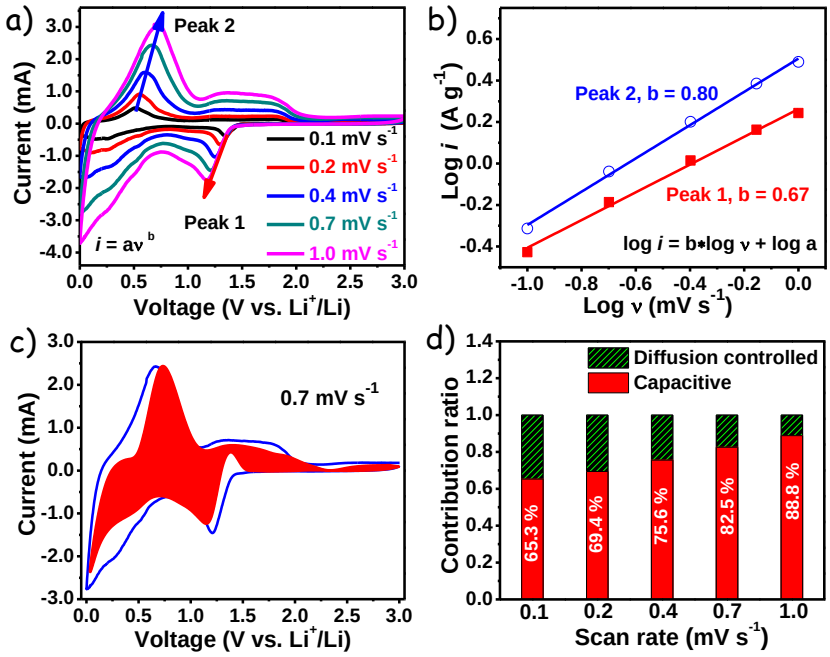

Figure 7. Li-ion storage performance of a SnS_2/CN/GP electrode: a) CV curves at the scan rates of 0.1, 0.2, 0.4, 0.7, and 1.0 mV s^{-1}. b) Linear fit of the logarithmic dependence between peak current density and scan rate at the anodic peak of 0.72 V and cathodic peak of 1.17 V. c) Capacitive contribution (red region) to the total current contribution at 0.7 mV s^{-1}. d) Normalized capacitive and diffusion-controlled contribution at the scan rates of 0.1, 0.2, 0.4, 0.7, and 1.0 mV s^{-1}.

Overall, based on the aforementioned analyses, the excellent performance of SnS_2/CN/GP anodes in LIBs was attributed to their hierarchical structure, which simultaneously allowed a large dispersion of the nanometric active material, a large porosity for electrolyte diffusion and a high electrical conductivity network for electron injection and extraction: 1) The small and thin SnS_2 NPLs provided more active sites than SnS_2 MFL, and a larger interface with the electrolyte, CN and GP, favoring Li reaction and intercalation kinetics;[89,90] 2) The highly porous and ultrathin CN provided suitable channels for Li-ions to rapidly diffuse through the electrode, and thus facilitate the electrochemical reaction. This effect was particularly important at high charge/discharge current densities; 3) The randomly distributed CN

within the SnS_2-NPL matrix acted as "cushion" and "spacer" to buffer the strain from volume changes, preventing the aggregation and detachment of SnS_2 during cycling; 4) GP provided avenues for efficient charge transport.

4. Conclusions

We developed a facile strategy to produce hierarchical SnS_2/CN/GP composites using SnS_2-NPL as active materials, porous CN to provide avenues for electrolyte diffusion and ease the volumetric expansion of SnS_2, and GP as "highways" for charge transport. Benefiting from this hierarchical structure and synergistic effects, an efficient ion/charge transportation and excellent lithium storage performance was achieved, with a capacity of 536.5 mAh g^{-1} and retention of ~99.7 % at a current density of 2.0 A g^{-1} after 400 cycles, and a high pseudocapacitance contribution of 88.8 % at a sweep rate of 1.0 mV s^{-1}. The hierarchical architecture here proposed can be used to promote performance in other energy storage devices.

Supporting Information

Supporting Information is available from **********

Acknowledgements

This work was supported by the European Regional Development Funds and by the Spanish Ministerio de Economía y Competitividad through the project SEHTOP (ENE2016-77798-C4-3-R). Y.Z. thanks China Scholarship Council for scholarship support (201606500001). This work was accomplished with the financial supported from the National Natural Science Foundation of China (no. 51771076) and (no. 51621001. the Foundation for Innovative Research Groups). Jun Liu acknowledges the support from Chinese Government the young "1000 plan", and thanks the projects of Guangzhou Science and Technology Plan (no. 201804010104) and Guangdong Province Public Interest Research and Capacity Building (no. 2017A010104004). Jordi Llorca is a Serra Húnter Fellow and is grateful to ICREA Academia program and GC 2017 SGR 128. X.H. thanks China Scholarship Council for scholarship support (201804910551). ICN2 acknowledge funding from Generalitat de Catalunya 2017 SGR 327 and the Spanish MINECO project ENE2017-85087-C3-3-R. ICN2 is supported by the Severo Ochoa program from Spanish MINECO (Grant No. SEV-2017-0706) and is funded by the CERCA Programme / Generalitat de Catalunya. Part of the present work has been performed in the framework of Universitat Autònoma de Barcelona Materials Science PhD program.

Conflict of Interest

The authors declare no conflict of interest.

References

[1] S. Martinet, Nanomaterials for rechargeable lithium batteries, Nanosci. Technol. 47 (2016) 471–512.

[2] M.N. Obrovac, V.L. Chevrier, Alloy negative electrodes for Li-ion batteries, Chem. Rev. 114 (2014) 11444–11502.

[3] J. Li, X. Xu, Z. Luo, C. Zhang, Y. Zuo, T. Zhang, P. Tang, M.F. Infante-Carrió, J. Arbiol, J. Llorca, J. Liu, A. Cabot, Co–Sn Nanocrystalline Solid Solutions as Anode Materials in Lithium-Ion Batteries with High Pseudocapacitive Contribution, ChemSusChem. 12 (2019) 1451–1458.

[4] L.X. Ding, G.R. Li, Z.L. Wang, Z.Q. Liu, H. Liu, Y.X. Tong, Porous Ni@Pt core-shell nanotube array electrocatalyst with high activity and stability for methanol oxidation, Chem. - A Eur. J. 18 (2012) 8386–8391.

[5] N.A. Kaskhedikar, J. Maier, Lithium storage in carbon nanostructures, Adv. Mater. 21 (2009) 2664–2680.

[6] X. Li, Y. Feng, M. Li, W. Li, H. Wei, D. Song, Smart Hybrids of Zn_2GeO_4 Nanoparticles and Ultrathin g-C_3N_4 Layers: Synergistic Lithium Storage and Excellent Electrochemical Performance, Adv. Funct. Mater. 25 (2015) 6858–6866.

[7] Y.S. Hu, R. Demir-Cakan, M.M. Titirici, J.O. Müller, R. Schlögl, M. Antonietti, J. Maier, Superior storage performance of a Si@SiOx/C nanocomposite as anode material for lithium-ion batteries, Angew. Chem. Int. Ed. 47 (2008) 1645–1649.

[8] C.K. Chan, H. Peng, G. Liu, K. McIlwrath, X.F. Zhang, R.A. Huggins, Y. Cui, High-performance lithium battery anodes using silicon nanowires, Nat. Nanotechnol. 3 (2008) 31–35.

[9] X.L. Wang, W.Q. Han, H. Chen, J. Bai, T.A. Tyson, X.Q. Yu, X.J. Wang, X.Q. Yang, Amorphous hierarchical porous GeO_x as high-capacity anodes for Li ion batteries with very long cycling life, J. Am. Chem. Soc. 133 (2011) 20692–20695.

[10] H. Kim, Y. Son, C. Park, J. Cho, H.C. Choi, Catalyst-free direct growth of a single to a few layers of graphene on a germanium nanowire for the anode material of a lithium battery, Angew. Chem. Int. Ed. 52 (2013) 5997–6001.

[11] W. Guo, Y. Wang, Q. Li, D. Wang, F. Zhang, Y. Yang, Y. Yu, SnO_2@C@VO_2 Composite Hollow Nanospheres as an Anode Material for Lithium-Ion Batteries, ACS Appl. Mater. Interfaces. 10 (2018) 14993–15000.

[12] S. Abouali, M. Akbari Garakani, J.K. Kim, Ultrafine SnO2 nanoparticles encapsulated in ordered mesoporous carbon framework for Li-ion battery anodes, Electrochim. Acta. 284 (2018) 436–443.

[13] Y. Liu, X.Y. Yu, Y. Fang, X. Zhu, J. Bao, X. Zhou, X.W. (David) Lou, Confining SnS_2 Ultrathin Nanosheets in Hollow Carbon Nanostructures for Efficient Capacitive Sodium Storage, Joule. 2 (2018) 725–735.

[14] Y. Wang, L. Huang, B. Li, J. Shang, C. Xia, C. Fan, H.-X. Deng, Z. Wei, J. Li, Composition-tunable 2D $SnSe_{2(1-x)}S_{2x}$ alloys towards efficient bandgap engineering and high performance (opto)electronics, J. Mater. Chem. C. 5 (2017) 84–90.

[15] L. Yin, R. Cheng, Q. Song, J. Yang, X. Kong, J. Huang, Y. Lin, H. Ouyang, Construction of nanoflower SnS_2 anchored on g-C_3N_4 nanosheets composite as highly efficient anode for lithium ion batteries, Electrochim. Acta. 293 (2019) 408–418.

[16] J.G. Wang, H. Sun, H. Liu, D. Jin, R. Zhou, B. Wei, Edge-oriented SnS_2 nanosheet arrays on carbon paper as advanced binder-free anodes for Li-ion and Na-ion batteries, J. Mater. Chem. A. 5 (2017) 23115–23122.

[17] J.B. Cook, H.S. Kim, T.C. Lin, C.H. Lai, B. Dunn, S.H. Tolbert, Pseudocapacitive Charge Storage in Thick Composite MoS_2 Nanocrystal-Based Electrodes, Adv. Energy Mater. 7 (2017) 1601283.

[18] Y. Zhao, Q. Pang, Y. Meng, Y. Gao, C. Wang, B. Liu, Y. Wei, F. Du, G. Chen, Self-Assembled CoS Nanoflowers Wrapped in Reduced Graphene Oxides as the High-Performance Anode Materials for Sodium-Ion Batteries, Chem. - A Eur. J. 23 (2017) 13150–13157.

[19] J. Johny, S. Sepulveda-Guzman, B. Krishnan, D. Avellaneda, S. Shaji, Facile and fast synthesis of SnS_2 nanoparticles by pulsed laser ablation in liquid, Appl. Surf. Sci. 435 (2018) 1285–1295.

[20] L. Fan, X. Li, X. Song, N. Hu, D. Xiong, A. Koo, X. Sun, Promising Dual-Doped Graphene Aerogel/SnS_2 Nanocrystal Building High Performance Sodium Ion Batteries, ACS Appl. Mater. Interfaces. 10 (2018) 2637–2648.

[21] Y. Zuo, Y. Liu, J. Li, R. Du, X. Yu, C. Xing, T. Zhang, L. Yao, J. Arbiol, J. Llorca, K. Sivula, N. Guijarro, A. Cabot, Solution-Processed Ultrathin SnS_2 -Pt Nanoplates for Photoelectrochemical Water Oxidation, ACS Appl. Mater. Interfaces. 11 (2019) 6918–6926.

[22] L. Wu, J. Zheng, L. Wang, X. Xiong, Y. Shao, G. Wang, J.H. Wang, S. Zhong, M. Wu, PPy-encapsulated SnS_2 Nanosheets Stabilized by Defects on a TiO_2 Support as a Durable Anode Material for Lithium-Ion Batteries, Angew. Chem. Int. Ed. 58 (2019) 811–815.

[23] B. Zhao, F. Chen, Z. Wang, S. Huang, Y. Jiang, Z. Chen, Lithiation-assisted exfoliation and reduction of SnS_2 to SnS decorated on lithium-integrated graphene for efficient energy storage, Nanoscale. 9 (2017) 17922–17932.

[24] X. Chen, Y. Huang, K. Zhang, X.S. Feng, M. Wang, Synthesis and high-performance of carbonaceous polypyrrole nanotubes coated with SnS_2 nanosheets anode materials for lithium ion batteries, Chem. Eng. J. 330 (2017) 470–479.

[25] H. Tang, X. Qi, W. Han, L. Ren, Y. Liu, X. Wang, J. Zhong, SnS_2 nanoplates embedded in 3D interconnected graphene network as anode material with superior lithium storage performance, Appl. Surf. Sci. 355 (2015) 7–13.

[26] H. Shang, Z. Zuo, L. Li, F. Wang, H. Liu, Y. Li, Y. Li, Ultrathin Graphdiyne Nanosheets Grown In Situ on Copper Nanowires and Their Performance as Lithium-Ion Battery Anodes, Angew. Chem. Int. Ed. 57 (2018) 774–778.

[27] B. Luo, Y. Hu, X. Zhu, T. Qiu, L. Zhi, M. Xiao, H. Zhang, M. Zou, A. Cao, L. Wang, Controllable growth of SnS_2 nanostructures on nanocarbon surfaces for lithium-ion and sodium-ion storage with high rate capability, J. Mater. Chem. A. 6 (2018) 1462–1472.

[28] J.G. Wang, H. Sun, H. Liu, D. Jin, X. Liu, X. Li, F. Kang, Triaxial Nanocables of Conducting Polypyrrole@SnS_2@Carbon Nanofiber Enabling Significantly Enhanced Li-Ion Storage, ACS Appl. Mater. Interfaces. 10 (2018) 13581–13587.

[29] D. Guan, J. Li, X. Gao, Y. Xie, C. Yuan, Growth characteristics and influencing factors of 3D hierarchical flower-like SnS_2 nanostructures and their superior lithium-ion intercalation performance, J. Alloys Compd. 658 (2016) 190–197.

[30] A. Bhaskar, M. Deepa, T.N. Rao, Tin Disulfide Nanoflowers versus Nanosheets as Anodes in Lithium-ion Batteries: How the Nanostructure Controls Performance, Electrochim. Acta. 184 (2015) 239–249.

[31] Y. Du, Z. Yin, X. Rui, Z. Zeng, X.J. Wu, J. Liu, Y. Zhu, J. Zhu, X. Huang, Q. Yan, H. Zhang, A facile, relative green, and inexpensive synthetic approach toward large-scale production of SnS_2 nanoplates for high-performance lithium-ion batteries, Nanoscale. 5 (2013) 1456–1459.

[32] Y. Wang, H. Li, P. He, E. Hosono, H. Zhou, Nano active materials for lithium-ion batteries, Nanoscale. 2 (2010) 1294–1305.

[33] J. Tang, X. Zhong, H. Li, Y. Li, F. Pan, B. Xu, In-situ and selectively laser reduced graphene oxide sheets as excellent conductive additive for high rate capability $LiFePO_4$ lithium ion batteries, J. Power Sources. 412 (2019) 677–682.

[34] W. Yao, S. Wu, L. Zhan, Y. Wang, Two-dimensional porous carbon-coated sandwich-like mesoporous SnO_2/graphene/mesoporous SnO_2 nanosheets towards high-rate and long cycle life lithium-ion batteries, Chem. Eng. J. 361 (2019) 329–341.

[35] A. Guo, E. Chen, B.R. Wygant, A. Heller, C.B. Mullins, Lead Oxide Microparticles Coated by Ethylenediamine-Cross-Linked Graphene Oxide for Lithium Ion Battery Anodes, ACS Appl. Energy Mater. 2 (2019) 3017–3020.

[36] L. Zhang, Y. Huang, Y. Zhang, W. Fan, T. Liu, Three-Dimensional Nanoporous Graphene-Carbon Nanotube Hybrid Frameworks for Confinement of SnS_2 Nanosheets: Flexible and Binder-Free Papers with Highly Reversible Lithium Storage, ACS Appl. Mater. Interfaces. 7 (2015) 27823–27830.

[37] K. Chang, Z. Wang, G. Huang, H. Li, W. Chen, J.Y. Lee, Few-layer SnS_2/graphene hybrid with exceptional electrochemical performance as lithium-ion battery anode, J. Power Sources. 201 (2012) 259–266.

[38] D. Cai, S. Wang, P. Lian, X. Zhu, D. Li, W. Yang, H. Wang, Superhigh capacity and rate capability of high-level nitrogen-doped graphene sheets as anode materials for lithium-ion batteries, Electrochim. Acta. 90 (2013) 492–497.

[39] Z.S. Wu, W. Ren, L. Xu, F. Li, H.M. Cheng, Doped graphene sheets as anode materials with superhigh rate and large capacity for lithium ion batteries, in: ACS Nano, 2011: pp. 5463–5471.

[40] E. Yoo, J. Nakamura, H. Zhou, N-Doped graphene nanosheets for Li-air fuel cells under acidic conditions, Energy Environ. Sci. 5 (2012) 6928–6932.

[41] Y. Fu, J. Zhu, C. Hu, X. Wu, X. Wang, Covalently coupled hybrid of graphitic carbon nitride with reduced graphene oxide as a superior performance lithium-ion battery anode, Nanoscale. 6 (2014) 12555–12564.

[42] Y. Zhang, A. Thomas, M. Antonietti, X. Wang, Activation of carbon nitride solids by protonation: Morphology changes, enhanced ionic conductivity, and photoconduction experiments, J. Am. Chem. Soc. 131 (2009) 50–51.

[43] J. Zhu, P. Xiao, H. Li, S.A.C. Carabineiro, Graphitic carbon nitride: Synthesis, properties, and applications in catalysis, ACS Appl. Mater. Interfaces. 6 (2014) 16449–16465.

[44] W.J. Ong, L.L. Tan, Y.H. Ng, S.T. Yong, S.P. Chai, Graphitic Carbon Nitride (g-C_3N_4)-Based Photocatalysts for Artificial Photosynthesis and Environmental Remediation: Are We a Step Closer to Achieving Sustainability?, Chem. Rev. 116 (2016) 7159–7329.

[45] X. Fan, L. Zhang, R. Cheng, M. Wang, M. Li, Y. Zhou, J. Shi, Construction of Graphitic C_3N_4-Based Intramolecular Donor-Acceptor Conjugated Copolymers for Photocatalytic Hydrogen Evolution, ACS Catal. 5 (2015) 5008–5015.

[46] X. An, C. Hu, H. Lan, H. Liu, J. Qu, Strongly Coupled Metal Oxide/Reassembled Carbon Nitride/Co-Pi Heterostructures for Efficient Photoelectrochemical Water Splitting, ACS Appl. Mater. Interfaces. 10 (2018) 6424–6432.

[47] Y. Zheng, J. Liu, J. Liang, M. Jaroniec, S.Z. Qiao, Graphitic carbon nitride materials: Controllable synthesis and applications in fuel cells and photocatalysis, Energy Environ. Sci. 5 (2012) 6717–6731.

[48] J. Li, X. Xu, Z. Luo, C. Zhang, X. Yu, Y. Zuo, T. Zhang, P. Tang, J. Arbiol, J. Llorca, J. Liu, A. Cabot, Compositionally tuned Ni_xSn alloys as anode materials for lithium-ion and sodium-ion batteries with a high pseudocapacitive contribution, Electrochim. Acta. 304 (2019) 246–254.

[49] M. He, M. Walter, K. V. Kravchyk, R. Erni, R. Widmer, M. V. Kovalenko, Monodisperse SnSb nanocrystals for Li-ion and Na-ion battery anodes: Synergy and dissonance between Sn and Sb, Nanoscale. 7 (2015) 455–459.

[50] L. Mei, C. Xu, T. Yang, J. Ma, L. Chen, Q. Li, T. Wang, Superior electrochemical performance of ultrasmall SnS_2 nanocrystals decorated on flexible RGO in lithium-ion batteries, J. Mater. Chem. A. 1 (2013) 8658–8664.

[51] W. Sun, X. Rui, D. Yang, Z. Sun, B. Li, W. Zhang, Y. Zong, S. Madhavi, S. Dou, Q. Yan, Two-Dimensional Tin Disulfide Nanosheets for Enhanced Sodium Storage, ACS Nano. 9 (2015) 11371–11381.

[52] L. Yin, R. Cheng, Q. Song, J. Yang, X. Kong, J. Huang, Y. Lin, H. Ouyang, Construction of nanoflower SnS_2 anchored on g-C_3N_4 nanosheets composite as highly efficient anode for lithium ion batteries, Electrochim. Acta. 293 (2019) 408–418.

[53] A. Rauf, M.S. Arif Sher Shah, J.Y. Lee, C.H. Chung, J.W. Bae, P.J. Yoo, Non-stoichiometric SnS microspheres with highly enhanced photoreduction efficiency for Cr(VI) ions, RSC Adv. 7 (2017) 30533–30541.

[54] H. Choi, J. Lee, S. Shin, J. Lee, S. Lee, H. Park, S. Kwon, N. Lee, M. Bang, S.B. Lee, H. Jeon, Fabrication of high crystalline SnS and SnS_2 thin films, and their switching device characteristics, Nanotechnology. 29 (2018) 215201.

[55] P. Zheng, Z. Dai, Y. Zhang, K.N. Dinh, Y. Zheng, H. Fan, J. Yang, R. Dangol, B. Li, Y. Zong, Q. Yan, X. Liu, Scalable synthesis of SnS_2/S-doped graphene composites for superior Li/Na-ion batteries, Nanoscale. 9 (2017) 14820–14825.

[56] S. Cao, J. Yu, G-C_3N_4-based photocatalysts for hydrogen generation, J. Phys. Chem. Lett. 5 (2014) 2101–2107.

[57] Z. Zhang, J. Huang, M. Zhang, Q. Yuan, B. Dong, Ultrathin hexagonal SnS_2 nanosheets coupled with g-C_3N_4 nanosheets as 2D/2D heterojunction photocatalysts toward high photocatalytic activity, Appl. Catal. B Environ. 163 (2015) 298–305.

[58] L. Jing, Y. Xu, Z. Chen, M. He, M. Xie, J. Liu, H. Xu, S. Huang, H. Li, Different Morphologies of SnS_2 Supported on 2D g-C_3N_4 for Excellent and Stable Visible Light Photocatalytic Hydrogen Generation, ACS Sustain. Chem. Eng. 6 (2018) 5132–5141.

[59] G. Wang, J. Peng, L. Zhang, J. Zhang, B. Dai, M. Zhu, L. Xia, F. Yu, Two-dimensional SnS_2@PANI nanoplates with high capacity and excellent stability for lithium-ion batteries, J. Mater. Chem. A. 3 (2015) 3659–3666.

[60] Y. Jiang, Y. Feng, B. Xi, S. Kai, K. Mi, J. Feng, J. Zhang, S. Xiong, Ultrasmall SnS_2 nanoparticles anchored on well-distributed nitrogen-doped graphene sheets for Li-ion and Na-ion batteries, J. Mater. Chem. A. 4 (2016) 10719–10726.

[61] B. Luo, Y. Hu, X. Zhu, T. Qiu, L. Zhi, M. Xiao, H. Zhang, M. Zou, A. Cao, L. Wang, Controllable growth of SnS_2 nanostructures on nanocarbon surfaces for lithium-ion and sodium-ion storage with high rate capability, J. Mater. Chem. A. 6 (2018) 1462–1472.

[62] J.G. Wang, H. Sun, H. Liu, D. Jin, R. Zhou, B. Wei, Edge-oriented SnS_2 nanosheet arrays on carbon paper as advanced binder-free anodes for Li-ion and Na-ion batteries, J. Mater. Chem. A. 5 (2017) 23115–23122.

[63] M.S.A. Sher Shah, A.R. Park, A. Rauf, S.H. Hong, Y. Choi, J. Park, J. Kim, W.J. Kim, P.J. Yoo, Highly interdigitated and porous architected ternary composite of SnS_2, g-C_3N_4 , and reduced graphene oxide (rGO) as high performance lithium ion battery anodes, RSC Adv. 7 (2017) 3125–3135.

[64] A. Bhaskar, M. Deepa, T.N. Rao, Tin Disulfide Nanoflowers versus Nanosheets as Anodes in Lithium-ion Batteries: How the Nanostructure Controls Performance, Electrochim. Acta. 184 (2015) 239–249.

[65] J. Zai, K. Wang, Y. Su, X. Qian, J. Chen, High stability and superior rate capability of three-dimensional hierarchical SnS_2 microspheres as anode material in lithium ion batteries, J. Power Sources. 196 (2011) 3650–3654.

[66] T.J. Kim, C. Kim, D. Son, M. Choi, B. Park, Novel SnS_2-nanosheet anodes for lithium-ion batteries, J. Power Sources. 167 (2007) 529–535.

[67] M.K. Song, Y. Zhang, E.J. Cairns, A long-life, high-rate lithium/sulfur cell: A multifaceted approach to enhancing cell performance, Nano Lett. 13 (2013) 5891–5899.

[68] X. Ji, S. Evers, R. Black, L.F. Nazar, Stabilizing lithium-sulphur cathodes using polysulphide reservoirs, Nat. Commun. 2 (2011) 325.

[69] Y. Liu, X.Y. Yu, Y. Fang, X. Zhu, J. Bao, X. Zhou, X.W. (David) Lou, Confining SnS_2 Ultrathin Nanosheets in Hollow Carbon Nanostructures for Efficient Capacitive Sodium Storage, Joule. 2 (2018) 725–735.

[70] X. Zhou, L. Yu, X.Y. Yu, X.W.D. Lou, Encapsulating Sn Nanoparticles in Amorphous Carbon Nanotubes for Enhanced Lithium Storage Properties, Adv. Energy Mater. 6 (2016) 1601177.

[71] Z. Zhang, H. Zhao, Z. Du, X. Chang, L. Zhao, X. Du, Z. Li, Y. Teng, J. Fang, K. Świerczek, (101) Plane-Oriented SnS_2 Nanoplates with Carbon Coating: A High-Rate and Cycle-Stable Anode Material for Lithium Ion Batteries, ACS Appl. Mater. Interfaces. 9 (2017) 35880–35887.

[72] L.L. Feng, G. Yu, Y. Wu, G.D. Li, H. Li, Y. Sun, T. Asefa, W. Chen, X. Zou, High-Index Faceted Ni_3S_2 Nanosheet Arrays as Highly Active and Ultrastable Electrocatalysts for Water Splitting, J. Am. Chem. Soc. 137 (2015) 14023–14026.

[73] L. Zhang, Y. Huang, Y. Zhang, W. Fan, T. Liu, Three-Dimensional Nanoporous Graphene-Carbon Nanotube Hybrid Frameworks for Confinement of SnS_2 Nanosheets: Flexible and Binder-Free Papers with Highly Reversible Lithium Storage, ACS Appl. Mater. Interfaces. 7 (2015) 27823–27830.

[74] X. Li, Y. Feng, M. Li, W. Li, H. Wei, D. Song, Smart Hybrids of Zn_2GeO_4 Nanoparticles and Ultrathin g-C_3N_4 Layers: Synergistic Lithium Storage and Excellent Electrochemical Performance, Adv. Funct. Mater. 25 (2015) 6858–6866.

[75] M. Shi, T. Wu, X. Song, J. Liu, L. Zhao, P. Zhang, L. Gao, Active Fe_2O_3 nanoparticles encapsulated in porous g-C_3N_4/graphene sandwich-type nanosheets as a superior anode for high-performance lithium-ion batteries, J. Mater. Chem. A. 4 (2016) 10666–10672.

[76] Z. Zhao, Y. Sun, F. Dong, Graphitic carbon nitride based nanocomposites: A review, Nanoscale. 7 (2015) 15–37.

[77] J. Duan, S. Chen, M. Jaroniec, S.Z. Qiao, Porous C_3N_4 nanolayers@n-graphene films as catalyst electrodes for highly efficient hydrogen evolution, ACS Nano. 9 (2015) 931–940.

[78] W. Liu, Y. Xia, W. Wang, Y. Wang, J. Jin, Y. Chen, E. Paek, D. Mitlin, Pristine or Highly Defective? Understanding the Role of Graphene Structure for Stable Lithium Metal Plating, Adv. Energy Mater. 9, (2019), 1802918.

[79] W. Liu, H. Li, J. Jin,Y. Wang, Z. Zhang, Z. Chen, Q. Wang, Y. Chen, E. Paek, D. Mitlin, Synergy of Epoxy Chemical Tethers and Defect-Free Graphene in Enabling Stable Lithium Cycling of Silicon Nanoparticles, Angew. Chem. Int. Ed. 58 (2019) 16743-16753.

[80] Y. Zuo, Y. Liu, J. Li, R. Du, X. Han, T. Zhang, J. Arbiol, N.J. Divins, J. Llorca, N. Guijarro, K. Sivula, A. Cabot, In Situ Electrochemical Oxidation of Cu_2S into CuO Nanowires as a Durable and Efficient Electrocatalyst for Oxygen Evolution Reaction, Chem. Mater. 31 (2019) 7732-7743.

[81] W. Wei, F.-F. Jia, K.-F. Wang, P. Qu, SnS_2/graphene nanocomposite: a high rate anode material for lithium ion battery. Chinese Chem. Lett. 28 (2017) 324–328.

[82] K. Yin, M. Zhang, Z. D. Hood, J. Pan, Y. S. Meng, M. Chi, Self-Assembled Framework Formed During Lithiation of SnS_2 Nanoplates Revealed by In Situ Electron Microscopy. Accounts Chem. Res. 50 (2017) 1513–1520.

[83] V. Augustyn, P. Simon, B. Dunn, Pseudocapacitive oxide materials for high-rate electrochemical energy storage, Energy Environ. Sci. 7 (2014) 1597–1614.

[84] L. Yang, X. Li, S. He, G. Du, X. Yu, J. Liu, Q. Gao, R. Hu, M. Zhu, Mesoporous Mo_2C/N-doped carbon heteronanowires as high-rate and long-life anode materials for Li-ion batteries, J. Mater. Chem. A. 4 (2016) 10842–10849.

[85] X. Xu, J. Liu, Z. Liu, J. Shen, R. Hu, J. Liu, L. Ouyang, L. Zhang, M. Zhu, Robust Pitaya-Structured Pyrite as High Energy Density Cathode for High-Rate Lithium Batteries, ACS Nano. 11 (2017) 9033–9040.

[86] X. Xu, J. Liu, J. Liu, L. Ouyang, R. Hu, H. Wang, L. Yang, M. Zhu, A General Metal-Organic Framework (MOF)-Derived Selenidation Strategy for In Situ Carbon-Encapsulated Metal Selenides as High-Rate Anodes for Na-Ion Batteries, Adv. Funct. Mater. 28 (2018) 1707573.

[87] T.-C. Liu, Behavior of Molybdenum Nitrides as Materials for Electrochemical Capacitors, J. Electrochem. Soc. 145 (1998) 1882. doi:10.1149/1.1838571.

[88] K. Zhang, M. Park, L. Zhou, G.H. Lee, J. Shin, Z. Hu, S.L. Chou, J. Chen, Y.M. Kang, Cobalt-Doped FeS_2 Nanospheres with Complete Solid Solubility as a High-Performance Anode Material for Sodium-Ion Batteries, Angew. Chem. Int. Ed. 55 (2016) 12822–12826.

[89] S. Liu, X. Lu, J. Xie, G. Cao, T. Zhu, X. Zhao, Preferential c-axis orientation of Ultrathin SnS_2 nanoplates on graphene as high-performance anode for li-ion batteries, ACS Appl. Mater. Interfaces. 5 (2013) 1588–1595.

[90] J.W. Seo, J.T. Jang, S.W. Park, C. Kim, B. Park, J. Cheon, Two-dimensional SnS_2 nanoplates with extraordinary high discharge capacity for lithium ion batteries, Adv. Mater. 20 (2008) 4269–4273.

TOC figure: